International Journal of Fracture 36: 243–257 (1988)

Three-dimensional crack tip deformation: an experimental study and comparison to HRR field

F.P. CHIANG and T.V. HAREESH
Laboratory for Experimental Mechanics Research, State University of New York at Stony Brook, Stony Brook, NY 11794-2300, USA

Received 7 October 1986; accepted in revised form 22 October 1987

Abstract. Three-dimensional deformation field in the vicinity of a blunt crack in a sheet of low-hardening material is determined using laser speckle and moiré techniques. Experimental results are compared with the HRR singularity field. A zone of dominant three-dimensional effects is mapped out ahead of the crack tip. Strain contours, elastic–plastic boundary and maximum shear strain trajectories are also plotted by numerically processing the experimental data.

1. Introduction

Displacement, strain and stress fields around an elastically or elasto-plastically deforming crack are often described by mathematical models based on a two-dimensional formulation. However, in reality these fields are likely to be three-dimensional. Furthermore, crack tips in most ductile materials undergo extensive yielding on loading and progressively get blunt prior to failure. This obviously affects the displacement, strain and stress fields in the immediate vicinity of the crack tip which is predicted to have singular behavior by the mathematical models. At the present the precise nature of the size and shape of this "immediate vicinity" remains obscure. One of the main purposes of this investigation is to have a better understanding of this aspect by quantifying the displacement and strain fields around a blunt crack tip.

For the case of brittle fracture in which the plasticity effect near the crack tip is small, the zone of 3-D deformation is estimated to be about half the size of the sheet thickness [1]. However, in ductile materials where the crack tip deformation is large and the plasticity effects significant, this aspect needs to be further investigated.

Attempts to experimentally study displacement and strain fields around crack tips in ductile materials have previously been made by many investigators. Kobayashi et al. [2], studied the transient strain fields around the crack tip in aluminum and magnesium alloys using photoprinted dot patterns. Employing the mismatch technique they measured the inplane displacement field and obtained the strain distribution by graphical differentiation. It was observed that the strength of the singularity is not $1/\sqrt{r}$ around the crack tip in the case of ductile materials. Underwood et al. [3], made studies on aluminum, brass and steel sheets with edge cracks. They adopted the classical interferometry in measuring residual out-of-plane displacements from polished specimens and employed ruled line gratings on different specimens to measure the crack opening strain ε_{22}. Consistent deviations were observed between the measured strains and their finite element calculations in the region close to the crack tip. Liu et al. [4, 5], also used line gratings to measure displacement

and strain fields in ductile sheets. Vasikovsky et al [22], have measured logitudinal and thickness strains close to the crack tip in steel samples by using scribed line gratings and replication techniques. However, none of these investigations have measured the complete 3-D displacement field ahead of a deforming crack.

In this investigation we have used two newly developed experimental techniques that could map all three displacement components simultaneously. We obtained the complete strain fields in the vicinity of a crack in several thin sheet specimens with either electro discharge machined (EDM) single edge notches or a fatigue crack. The results are consistent with one another. We also compared the results to the so-called plane stress HRR singular field showing a region of deviation.

2. Brief description of the experimental methods

Two methods [6–8] with complimenting ranges of application, were employed. The first method is a combined laser speckle-moiré method [6], of which the experimental arrangement is as shown in Fig. 1.

A He–Ne laser beam is first expanded by a microscopic objective, and then collimated by a field lens before it impinges upon a line-grating. The regular and diffracted wavefronts are collected by a second field lens which forms the diffraction spectrum of the grating at its focal plane in the form of a series of equally spaced bright dots called diffraction orders. All the orders are blocked by a mask except the ± 1 orders which are collected by a third field lens to form two nearly collimated beams with an angle 2α between them to impinge upon the spectrum. Within the intersecting beams there exists a standing wave of period (or pitch)

$$p = \frac{1}{2 \sin \alpha}, \tag{1}$$

where λ is the wavelength.

When a specimen is placed in this field it is covered by two patterns. One is the projected grating from the standing wave with a pitch

$$p' = \frac{\lambda}{2 \sin \alpha \cos \beta}, \tag{2}$$

where β is the angle between the normal to the plate and the optical axis of the projection system. Another is a laser speckle field which is a random interference pattern resulting from the mutual interference of the numerous reflected wavelets. The latter has been exploited in recent years as an effective means of measuring displacement and strain fields in solids [9] and velocity distributions in fluids [10]. This complex optical field on the specimen can be photographed before and after deformation via double exposure on the same photographic plate. This so-called specklegram can then be optically processed to yield various displacement contours.

To facilitate the recording of high frequency signals in this complex optical field we have used a mask with four apertures at the pupil plane of the lens [11]. A typical recording through such a system is shown in Fig. 1(b) (after enlargement). It consists of the coarse

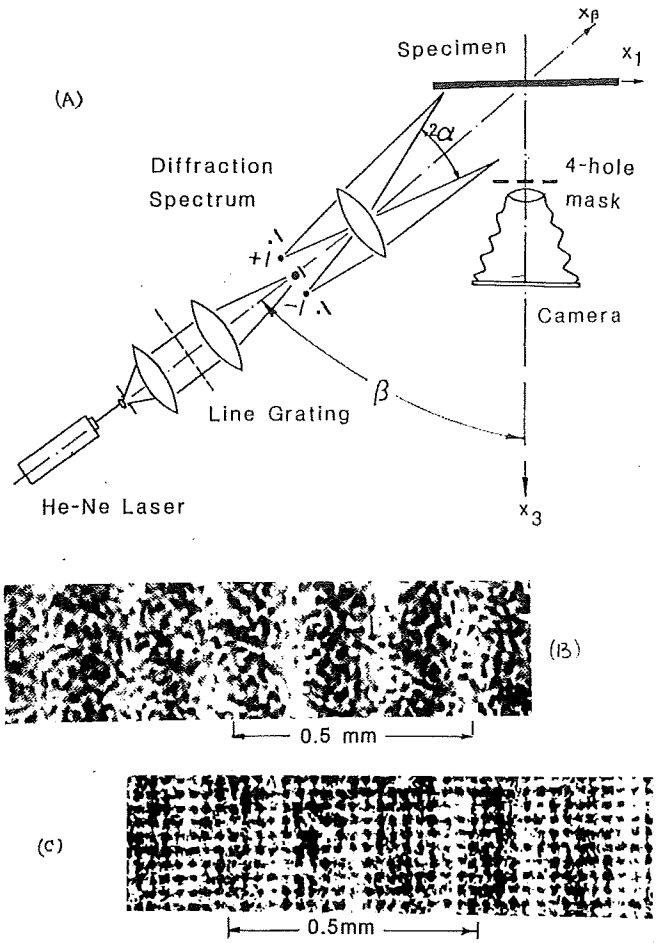

Fig. 1. Two experimental methods for mapping 3-D displacement fields at crack tip: (a) optical arrangement; (b) speckle-grating pattern formed on the specimen surface by method I; (c) combined gratings formed on specimen surface by method II.

grating due to the interfering standing waves, the random laser speckle pattern and the fine cross-grating structure within speckles as a result of the four-apertures.

Upon deformation the specimen's inplane displacement (u_1 and u_2) is encoded in the displacement of the random speckles whereas its out-of-plane displacement is embedded in the distortion of the projected grating lines. All these can be delineated in the form of contour fringes of displacement component through a process called optical spatial filtering [12]. A system for performing filtering is schematically shown in Fig. 2. The specklegram is placed in a coherent light field and its spatial frequency spectrum is displayed at the Fourier transform plane of the first field lens. By appropriately selecting the diffraction orders at this plane to be collected by the second field lens, contour fringes of u_1, u_2 and u_3 (i.e., displacements in the x_1, x_2 and x_3 directions, respectively) can be obtained. The governing equations are

$$u_1 = \frac{N\lambda f}{r_1} \quad N = 0, \pm 1, \pm 2, \ldots \tag{3}$$

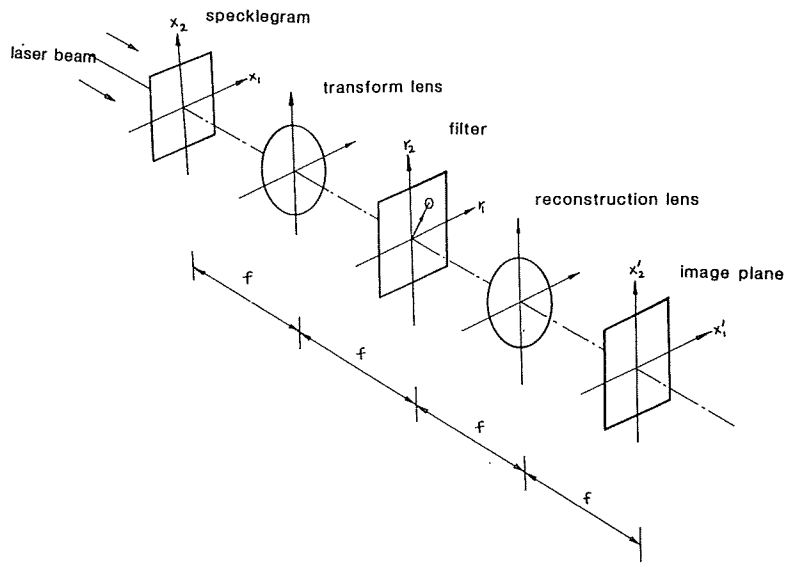

Fig. 2. Optical arrangement for whole field Fourier filtering.

$$u_2 = \frac{N'\lambda f}{r_2} \qquad N' = 0, \pm 1, \pm 2, \ldots \tag{4}$$

$$u_3 = \frac{N''\lambda}{4 \tan \alpha \sin \beta} \qquad N'' = 0, \pm 1, \pm 2, \ldots \tag{5}$$

where f is the focal length of the Fourier transform lens, $r(r_1, r_2)$ the position vector of the filtering hole at the transform plane. The u_3 fringe pattern is obtained by collecting both of the diffraction orders from the projected grating to form a frequency doubled deformed grating at the image plane and superimposed on a reference grating.

The aforementioned technique has a relatively high sensitivity. When the strain at the crack tip becomes excessive, the laser speckles tend to decorrelate resulting in poor fringe contrast. To compensate for this difficulty we compliment it with a combined in-plane and projection moiré method [7] which can map large strains. The experimental setup for this method is essentially the same as shown in Fig. 1 except that the specimen's surface is printed with a cross grating using a photoengraving process. Recording is done through ordinary photography in that no special mask is placed at the pupil plane of the recording lens. An enlargement of a typical recording is shown in Fig. 1(c). Optical spatial filtering is again utilized in a way similar to that of the speckle-grating method to generate u_1, u_2 and u_3 fringes individually. The governing equations are the same as (3), (4) and (5) except that a single parameter p (pitch of the printed cross-grating) replaces the constants $\lambda f/r_1$ and $\lambda f/r_2$ in (3) and (4).

The experiments

The material selected for this investigation was Al 6061-T6. Single edge notch (SEN) specimens were made from 3.2 mm thick sheets of the material with dimensions shown in

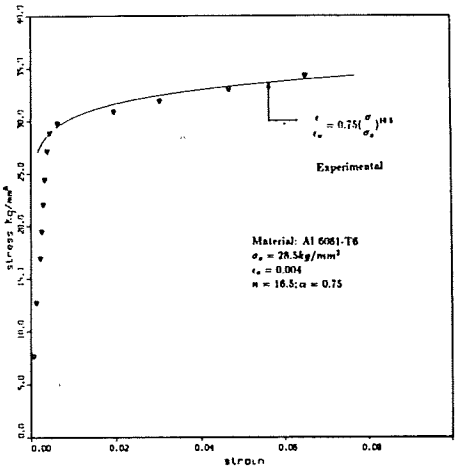

(a)

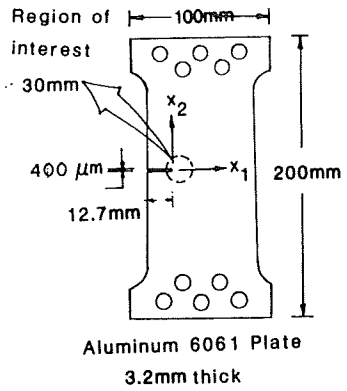

(b)

Fig. 3. Single edge notch specimen and the material characteristics curve.

Fig. 3(b). The specimens were subjected to far field tensile load and the width to thickness ratio of 24 resulted in an essentially plane stress state. Cracks were cut either by EDM processes or created by fatigue loading a notched specimen. The longitudinal direction (i.e., the loading direction) is aligned with the rolling direction of the sheet. The material was calibrated using a simple tension test resulting in a true stress-true strain curve shown in Fig. 3(a). Ramberg–Osgood relation was used to fit the curve, i.e.,

$$\frac{\varepsilon}{\varepsilon_0} = \frac{\sigma}{\sigma_0} + \alpha\left(\frac{\sigma}{\sigma_0}\right)^n \tag{6}$$

where σ_0 is the yield stress, ε_0 yield strain, n material hardening index and α a constant. The calibrated material parameters including Young's modulus are indicated in Fig. 3.

The first set of experiments were done using the laser speckle-moiré method. Typical fringe patterns are as shown in Fig. 4. Because of their high sensitivity the speckle fringes (i.e., the u_1 and u_2-field fringes) were obtained from incremental loadings. The ones in Fig. 4 were obtained when the far field stress σ_∞ was increased from 55 to 68 percent of the yield stress σ_0. The moiré pattern (i.e., the u_3-field fringes), however, was obtained using the total load.

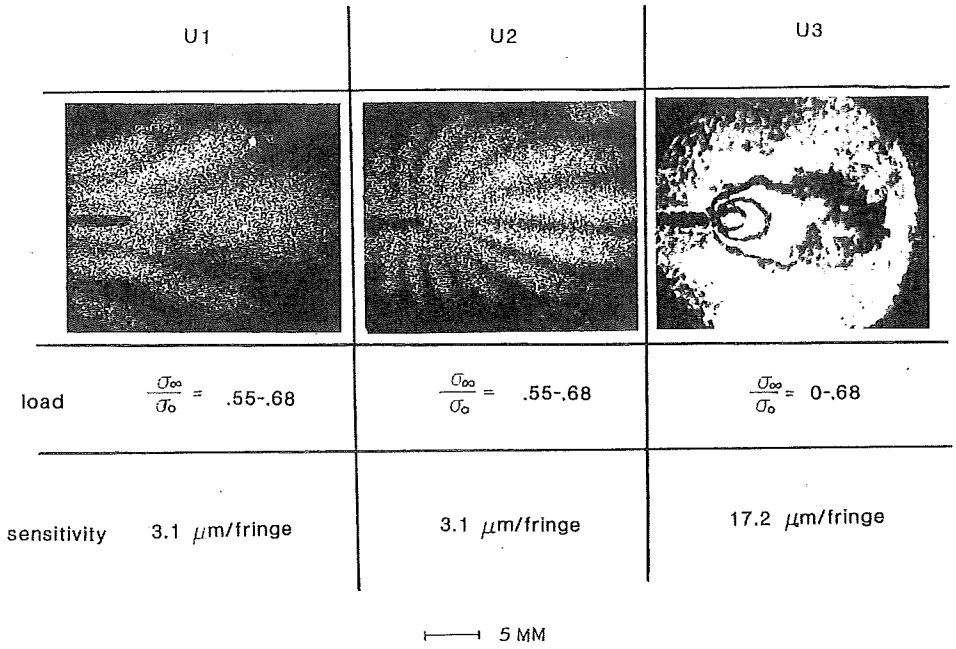

Fig. 4. Speckle and projection moiré patterns obtained from method I showing displacement contours of u_1, u_2 and u_3 along Cartesian directions, respectively.

The sensitivity of the methods as represented by displacement per fringe are also listed in the figure. An interesting phenomenon is observable at the crack tip in the speckle fringe patterns: there is a region within which the speckle fringes are blurred. This was the region where the specimen experienced large plastic deformation resulting in speckle decorrelation [13]. The moiré fringes, on the other hand, manifest themselves clearly in this domain. To compensate the lost information in this region we tested new specimens using the combined in-plane and projection moiré method described in the preceding section. The cross-grating photoengraved onto the specimen surface had a spatial frequency of 40 lines/mm resulting in a sensitivity of 25.4 μm per fringe. Typical fringe patterns for the three displacement components are shown in Fig. 5. Each row of fringe patterns shows the three displacement component fields at each stage of loading. While the global state of the specimen was plane stress, it was evident from the fringe patterns that a state of 3-D deformation existed in a region near the crack tip.

4. Experimental results and comparison to HRR field

As a measure we selected for comparison the plane stress version of the so-called HRR singularity field, developed by Hutchinson [14, 15], Rice and Rosengren [16]. It assumes a Ramberg–Osgood stress-strain behavior as given by (6). Deformation theory of plasticity is invoked resulting in predominant strain-stress relationship of the form

$$\varepsilon_{ij} = (3/2)\alpha\sigma_e^{n-1}(s_{ij}/E), \tag{7}$$

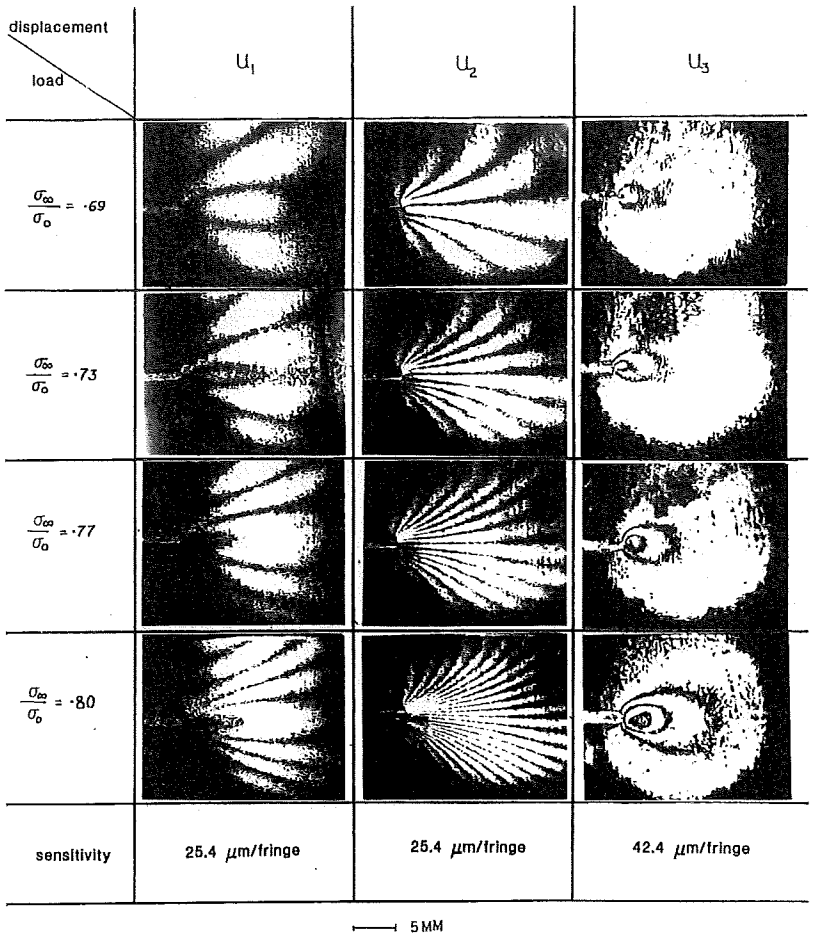

Fig. 5. In-plane and projection moiré patterns obtained from method II showing displacement contours of u_1, u_2 and u_3 along Cartesian directions, respectively.

where E is the Young's modulus, $s_{ij} = \sigma_{ij} - (1/3)\sigma_{kk}\delta_{ij}$ is the stress deviator of σ_{ij}. Von Mises yield criterion is introduced in the form of effective stress $\sigma_e = (\frac{3}{2}s_{ij}s_{ij})^{1/2}$. Based on the stress function approach, field equations in the vicinity of the crack undergoing plane stress deformation are derived as

$$\begin{aligned} \sigma_{ij}(r, \theta) &= \sigma_0 C^{1/n+1}\, \tilde{\sigma}_{ij}(\theta, n) \\ \varepsilon_{ij}(r, \theta) &= \alpha\varepsilon_0 C^{n/n+1} \tilde{\varepsilon}_{ij}(\theta, n) \\ u_i(r, \theta) &= \alpha\varepsilon_0 r C^{n/n+1} \tilde{u}_i(\theta, n), \end{aligned} \tag{8}$$

where

$$C = \left(\frac{J}{\alpha\sigma_0\varepsilon_0 I_n r}\right).$$

In these equations J is Rice's J-integral given by,

$$J = \int_\Gamma W \, dx_2 - \sigma_{ij} n_j u_{i,x_1} \, ds, \quad \text{where } W = \int^{\varepsilon} \sigma_{ij} \, d\varepsilon_{ij}.$$

Here, n_j represents the unit vector normal to the contour Γ and (x_1, x_2) are the Cartesian coordinates with the origin at the crack tip. $\tilde{\sigma}_{ij}$, $\tilde{\varepsilon}_{ij}$ and $\tilde{u}_i$ are functions of the polar coordinate θ and hardening index n and I_n is a constant dependent on n. A detailed tabulation of all these constants is given by Shih [17]. In our comparisons the displacements were normalized using the crack tip opening displacement δ_t defined for a blunt crack as [17],

$$\delta_t = (\alpha \varepsilon_0)^{1/n} D_n (J/\sigma_0) \tag{9}$$

where D_n is a constant dependent on the hardening index n of the material.

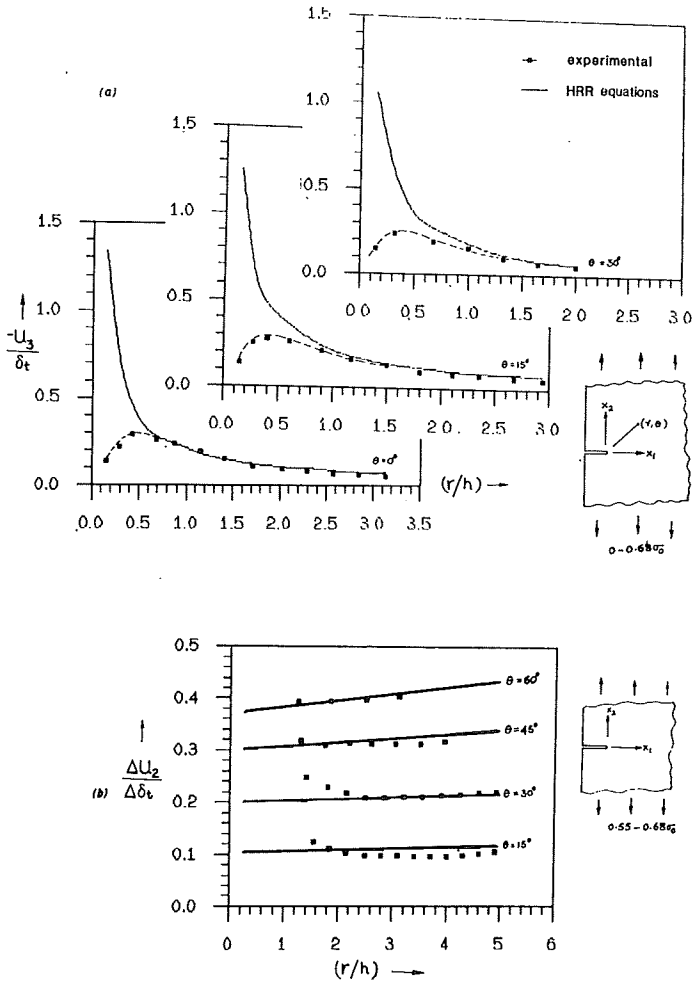

Fig. 6. Comparison between HRR field and results obtained by experimental method I: (a) comparison of out-of-plane displacement u_3, and (b) comparison of in-plane displacement u_2.

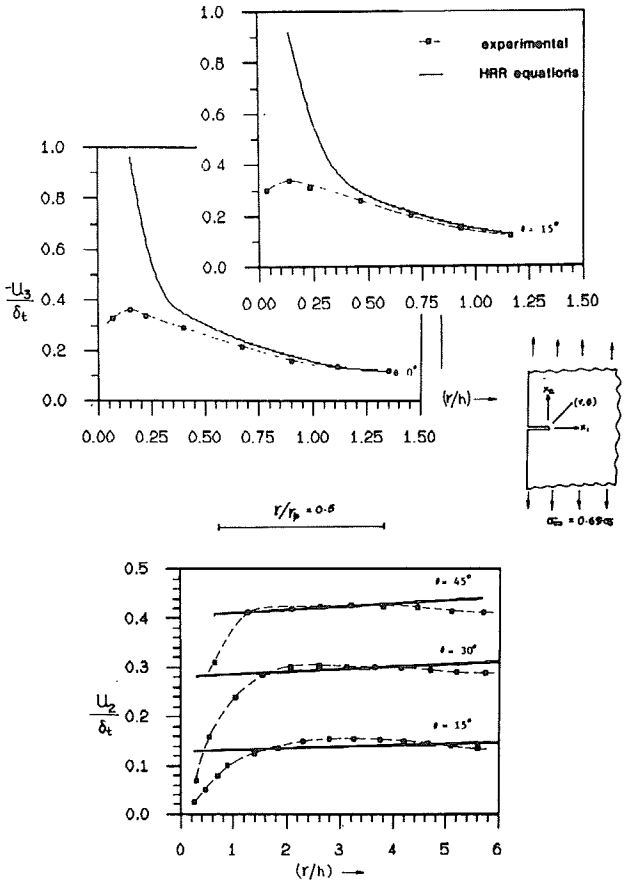

Fig. 7. Comparison between HRR field and results obtained by experimental method II for $\sigma_\infty = 0.69\sigma_0$: (a) comparison of out-of-plane displacement u_3, and (b) comparison of in-plane displacement u_2. (Applied load to limit load ratio, $(P/P_{\text{lim}}) = 0.95$).

Figure 6(a) shows the comparison of the out-of-plane displacement u_3 between the experimental results obtained from the speckle-moiré method (method I) and the theoretical values derived from the incompressibility condition

$$\varepsilon_{33}^p = \frac{-2u_3(r, \theta)}{h} = -(\varepsilon_{rr}^p + \varepsilon_{\theta\theta}^p), \tag{10}$$

where h is the thickness of the plate. In applying this equation we have assumed that the state of stress prevails and ε_{33}^p is the average strain across the thickness. The comparison between experimental and theoretical values of u_2 is shown in Fig. 6(b). In this figure the incremental Δu_2 and $\Delta\delta_t$ for the load difference of $0.55\sigma_0 - 0.68\sigma_0$ were used because the inplane displacement was obtained by the speckle-grating method which has a sensitivity one order of magnitude higher than that of the projection moiré method used for obtaining u_3. A large deformation would result in speckle decorrelation.

Similar plots were made between the HRR field and the experimental result obtained by the combined moiré method (method II), and they are shown in Fig. 7 for the loading

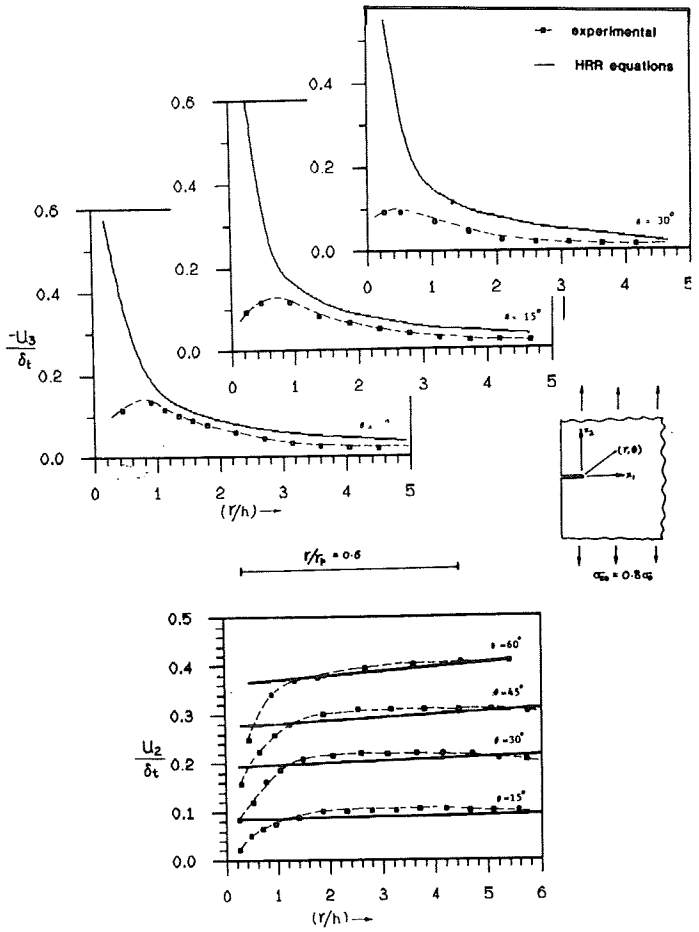

Fig. 8. Comparison between HRR field and the results obtained by experimental method II for $\sigma_\infty = 0.80\sigma_0$: (a) comparison of u_3 and (b) comparison of u_2. (Applied load to limit load ratio, $(P/P_{\text{lim}}) = 1.07$).

$\sigma_\infty = 0.69\sigma_0$, and in Fig. 8 for the loading $\sigma_\infty = 0.8r_0$. In all these plots the experimental δ_t (or $\Delta\delta_t$) was obtained by counting the u_2 (or Δu_2) fringes (and multiplying the sensitivity factor) between θ approximately equal to $-135°$ and $+135°$ with respect to the deformed crack tip [17]. Because of relatively few fringes, we did not do a comparison between the experimental and theoretical u_1 distribution. In these comparisons, Irwin's plastic zone length parameter r_p is also shown for completeness. r_p was calculated based on small scale yielding assumption using corrections to the crack length parameters [23]. However, it should be noted that the presented cases deal with situations in which the specimen had been subjected to loads near or beyond the limit load for the chosen geometry. As a consequence direct interpretation of the results in terms of r_p, which is a small scale yielding parameter, is not appropriate.

A number of interesting observations can be made from these plots. First of all the out-of-plane displacement u_3 at the crack tip is finite (as one would expect) as against singular prediction by the HRR model. The maximum out-of-plane displacement seems to occur at some distance away from the blunt crack tip. The elastic counterpart of this phenomenon was predicted by Yang and Freund [18] and experimentally observed by Rosakis and

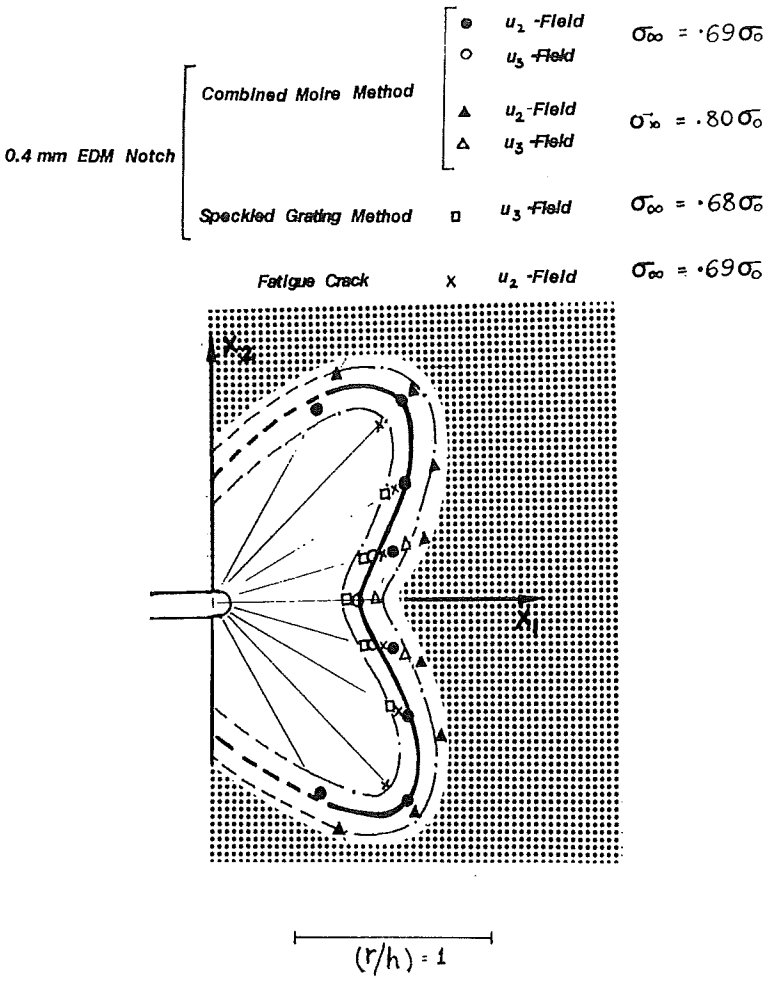

Fig. 9. Combined result showing 3-D zone (unshaded region) at crack tip where the HRR predictions and experimental results deviate significantly. Dotted lines are extrapolations. The band indicates the uncertainty in the data.

Ravi Chander [1]. More importantly one sees a general trend from these plots that within a small region near the blunt crack tip the predictions based on the HRR model deviate substantially from the experimental measurements. This is the result of strong three dimensional deformation near the crack tip in a plate of finite thickness. The HRR field on the other hand is derived based on a 2-D (plane stress) approximation. Furthermore, HRR equations are based on small strain formulations and in reality large deformations occur in the close vicinity of the blunting crack tip. If we define the boundary of this 3-D zone as being where the experimental and theoretical results differ by $\pm 0.025(u_{2\text{or}3}/\delta_t)$ we can have the 3-D zone mapped out as shown in Fig. 9 which is the composite result of six sets of experimental data. (The u_2-field results from method I were not used because of the lack of fringe clarity near the crack tip.)

The experimental data presented in Figs. 6–8 were from artificially produced cracks using the electro-discharge machining process. The cracks had a finite radius of about 400 μm. To

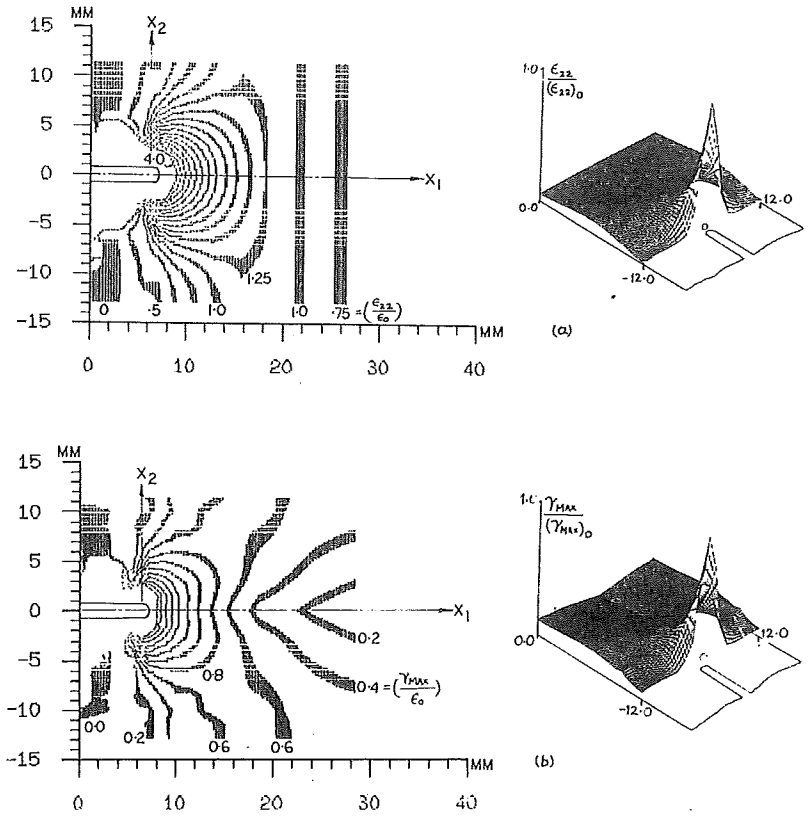

Fig. 10. Strain contours for $\sigma_\infty = 0.69\sigma_0$ from experimental data: (a) normalized opening strain $\varepsilon_{22}/\varepsilon_0$ and surface representation of ε_{22} normalized to unity at the crack tip; (b) normalized shearing strain $\gamma_{max}/\varepsilon_0$ and surface representation of γ_{max} normalized to unity at the crack tip.

check whether the same phenomenon would be observed from sharp cracks, we performed an experiment using a fatigue generated crack. Similar results were obtained and the corresponding points are also included in the results shown in Fig. 9. It is seen that the 3-D zone is in the shape of a butterfly wing and has a range of about 0.8 times the thickness of the plate along the crack direction to about 1.5 times the thickness along approximately ± 45 deg directions. It should be noted that we did not have reliable experimental data beyond ± 60 deg. Thus the zone boundary beyond that is a mere extrapolation and plotted in dotted lines. The two neighbouring lines parallel to the solid line indicate the uncertainty of the experimental data. The results in Fig. 9 should be viewed with the perspective that the HRR field is a 2-D analysis based on the small strain assumption. The zone wherein the experimental and theoretical results deviate substantially is a region where the strains are large as well as triaxial.

In order to have a better appreciation of the deformation field in the vicinity of the crack we proceeded to calculate the strain distributions from the displacement values. To this end the fringe patterns (from method II) due to $\sigma_\infty = 0.69\sigma_0$ and $\sigma_\infty = 0.8\sigma_0$ were digitized and numerically differentiated with respect to the spatial co-ordinates x_1 and x_2 using smoothed cubic spline approximations [19]. The strain components were then calculated at about 400 nodal points of a 2-D virtual grid in the crack tip region using the following strain-displacement

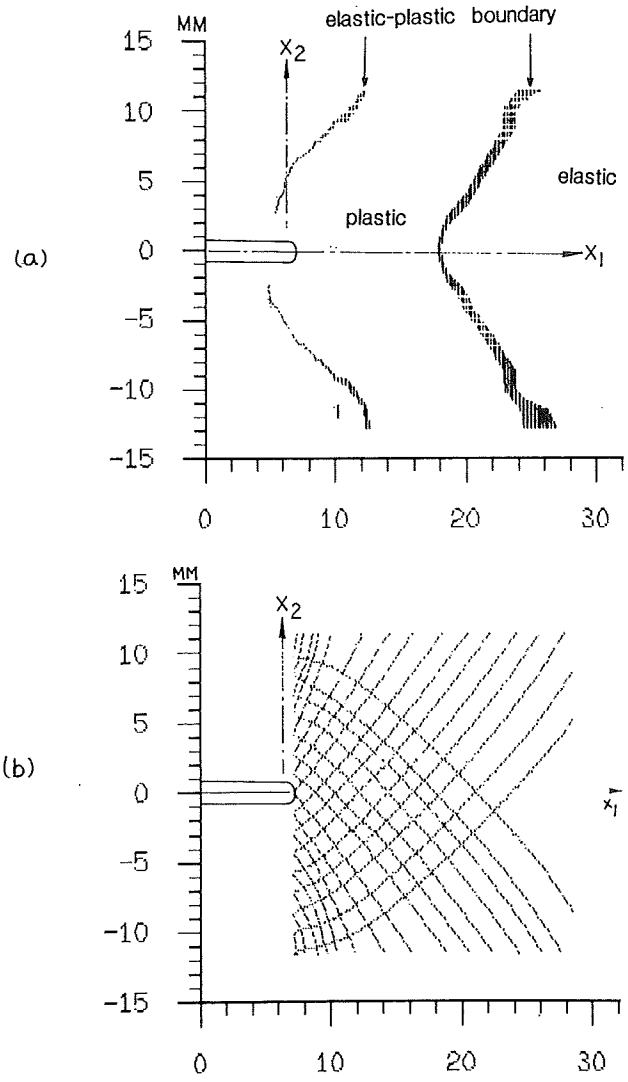

Fig. 11. (a) Experimental elastic-plastic boundary in the vicinity of the blunt crack for $\sigma_\infty = 0.69\sigma_0$. (b) Trajectories of maximum shear strain obtained from experimental data for $\sigma_\infty = 0.80\sigma_0$.

relations:

$$\varepsilon_{11} = (\partial u_1/\partial x_1): \quad \varepsilon_{22} = (\partial u_2/\partial x_2)$$

and

$$\gamma_{12} = (\partial u_2/\partial x_1) + (\partial u_1/\partial x_2). \tag{11}$$

From these components, maximum shear strain γ_{max} and effective strain ε_e were calculated using

$$\gamma_{max} = \left[\left(\frac{\varepsilon_{11} - \varepsilon_{22}}{2}\right)^2 + \varepsilon_{12}^2\right]^{1/2} \tag{12}$$

$$\varepsilon_e = \frac{\sqrt{2}}{2(1+\nu)}[(\varepsilon_{11} - \varepsilon_{22})^2 + (\varepsilon_{22} - \varepsilon_{33})^2 + (\varepsilon_{33} - \varepsilon_{11})^2 + 1.5\gamma_{12}^2]^{1/2}. \tag{13}$$

By employing a 2-D parabolic interpolation using isoparametric elements, strain at any specified location in the vicinity of the crack was calculated by

$$\varepsilon = N_p N_q \varepsilon_{pq}, \tag{14}$$

where ε_{pq} is the nodal strain value and N_p and N_q are the corresponding shape functions [20]. The resulting strain contours for ε_{22} and γ_{max} are shown in Fig. 10. Very high strain gradients exist in the region close to the crack tip within about 1.5 times the thickness of the plate. Beyond this the distribution is essentially a small linear variation. In Fig. 11(a) ε_e the contours with a strain value equal to the yield strain ε_0 is shown. If one adopts the von Mises yield criterion this contour is simply the elastic-plastic boundary of the region surrounding the crack tip. It should be noted that since we did not have data beyond the processed region, the upper and lower parts of the boundary have been cut off. It corresponds to shear type plastic zone as evidenced by the 45 deg shear lips observed on specimen failure. Plastic zone of similar shape has been observed by a chemical etching process [21].

From the known strain components maximum shear strain trajectories can be produced by using a simple algorithm and the results are shown in Fig. 11(b). The pattern is akin to the classical slip-line field. We note that for a blunt crack with a semi-circular crack front in an elastic-perfectly plastic material under strain, the slip line field has a shape of a logarithmic spiral as shown by Rice and Johnson. However, a direct comparison of the two is not appropriate because the present study deals with a state of plane stress in a strain hardening material.

5. Conclusions

By employing two newly developed experimental techniques we have succeeded in mapping the three-dimensional displacement field in the vicinity of a blunt crack in Al 6061-T6 SEN specimens undergoing large plastic deformation. The results are compared with the HRR singularity field showing a region near the crack tip where substantial deviations exist due to the finite thickness of the plate resulting in a three-dimensional crack tip field. This butterfly wing shaped zone extends from 0.8 times the plate thickness in the crack direction to about 1.5 times in ± 45 deg directions. Essentially the same phenomenon exists in both EDM cut notches and fatigue cracks. From the displacement values, strains are calculated using a routine of cubic spline approximation. Strain contours and maximum shear strain trajectories are plotted. Experimental elastic–plastic boundary based on Von Mises yield condition is also obtained.

Acknowledgements

We would like to thank, for the financial support provided, the Office of Naval Research (Mechanics Division) through contract no. N0001482k0566 (Dr Y. Rajapakse, Scientific Officer) and National Science Foundation (Solid and Geo-Mechanical Program) grant no. MEA8403912 (Dr K. Thirumalai, Program Director). Preliminary results of this work were presented at the 1985 [6] and 1986 [7] Spring meetings of the Society of Experimental Mechanics and Summaries published in the proceedings.

References

1. A.J. Rosakis and K. Ravi Chander, "On crack tip stress state: An experimental evaluation of three dimensional effects", Report SM84-2, California Institute of Technology, Pasadena, CA (1984).
2. A.S. Kobayashi, D.O. Harris and W.L. Engstrom, *Experimental Mechanics* 7 (1967) 434–440.
3. J.H. Underwood, J.L. Swedlow and D.P. Kendall, *Engineering Fracture Mechanics* 2 (1971) 183–196.
4. H.W. Liu, W.J. Gavigan and J.S. Ke, *International Journal of Fracture Mechanics* 6 (1970) 41–53.
5. H.W. Liu and J.S. Ke, *Moiré Method in Experimental Techniques in Fracture Mechanics*, Vol. 2, A.S. Koyayashi (ed.) SESA Monograph No. 2 (1975) Chapter IV.
6. F.P. Chiang and T.V. Hareesh, in *Proceedings 1985 SEM spring Conference on Experimental Mechanics*. Las Vegas (1985) 112.
7. F.P Chiang and T.V. Hareesh, in *Proceedings 1986 SEM spring Conference on Experimental Mechanics* (1986) 782.
8. F.P. Chiang and T.V. Hareesh, "Techniques for 3-D crack tip displacement measurement" in preparation.
9. F.P. Chiang,*Solid Mechanics Archives*, 3, 1–32 (1978) 27–58.
10. T.D. Duderār and P.G. Simpkins, *Optical Engineering* 21 (1982) 396–339.
11. F.P. Chiang and R.P. Ketan, *Applied Optics* 18 (1979) 2175–2186.
12. F.P. Chiang, *Experimental Mechanics* 6 (1979) 523–526.
13. D.W. Li, J.B. Chen and F.P. Chiang, *JOSA* 2 (1985) 657–666.
14. J.W. Hutchinson, *Journal of Mechanics and Physics of Solids* 16 (1968) 13–31.
15. J.W. Hutchinson, *Journal of Mechanics and Physics of Solids* 16 (1968) 337–347.
16. J.R. Rice and G.F. Rosengren, *Journal of Mechanics and Physics of Solids* 16 (1968) 1–12.
17. C.F. Shih, "Tables of HRR singular field quantities", Rep. No. MRL E-147, Materials Research Laboratory, Brown University, Providence (1983).
18. W. Yang and L.B. Freund, "Transverse shear effects for through cracks in an elastic plate", Brown University report (1984).
19. D.G. Berghaus and J.P. Cannon, *Experimental Mechanics* (1977) 177–183.
20. R.D. Cook, *Concepts and Applications of Finite Element Analysis*, 2nd ed., John Wiley & Sons (1981).
21. G.T. Hahn and A.R. Rosenfield, *Acta Metallurgica* 13 (1965) 293–306.
22. O. Vasikovsky, *International Journal of Fracture* 10 (1974) 141–166.
23. M.F. Kanninen and C.H. Popelar, *Advanced Fracture Mechanics*, Oxford Engineering Science Series 15, Oxford University Press, New York (1985).

Résumé. On détermine le champ de déformation des dimensions au voisinage d'une fissure arrondie dans un feuillard d'un matériau à faible consolidation en utilisant un faisceau laser et la technique des moirés. Les résultats des essais sont comparés avec ce que fournit un champ de singularité HRR. On procède à un mapping d'une zone à effets tridimensionnels dominants en amont de l'extrémité de la fissure. Les contours des déformations, la frontière élastique-plastique et les trajectoires de déformations maximum de cisaillement sont également portées en diagramme par un traitement numérique des données expérimentales.